ACS OMEGA

Open Access

http://pubs.acs.org/journal/acsodf

Article

Powder Synthesis and Characterization of $Al_{0.5}CoCrFeNi$ High-Entropy Alloy for Additive Manufacturing Prepared by the Plasma Rotating Electrode Process

Yanchun Li, Yi Sui, Yicheng Feng,* Yu Zhang, Yan Li, Meihui Song, Shulin Gong, and Yang Xie*

Cite This: *ACS Omega* 2024, 9, 18358−18365

Read Online

ACCESS | Metrics & More | Article Recommendations | Supporting Information

ABSTRACT: The $Al_{0.5}CoCrFeNi$ high-entropy alloy powder was produced by using a plasma rotating electrode process. The morphology, microstructure, and physical properties of the powder were characterized. The powder exhibited a smooth surface and a narrow particle size distribution with a single peak. The relationships between particle size and secondary dendrite arm space as well as cooling rate were evaluated as follows: $\lambda = 0.0105d + 0.062$ and $v_c = 4.34 \times 10^{-5}d^{-2} + 2.62 \times 10^{-2}d^{-3/2}$, respectively. The $Al_{0.5}CoCrFeNi$ powder mainly consisted of fcc + bcc phases. As the powder particle size decreased, the microstructure of the powder changed from dendritic to columnar or equiaxed, along with a decrease in the fcc content and an increase in the bcc content. The tap density (4.76 g cm^{-3}), flowability (15.01 s × 50 g^{-1}), oxygen content (<300 ppm), and sphericity (>94%) of the powder indicated suitability for additive manufacturing.

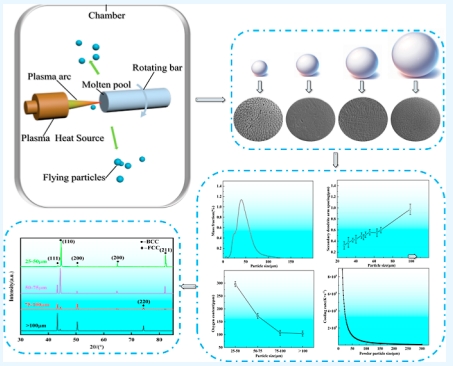

1. INTRODUCTION

High-entropy alloys (HEAs), consisting of five or more major elements with equal or almost equal molar fractions, were proposed in 2004.[1] Compared to traditional metal materials, HEAs possess numerous significant advantages, including exceptional high-temperature strength, excellent strength-plasticity, and high−low-temperature tensile strength.[2−4] Nowadays, HEAs are mainly prepared by casting, metallurgical sintering, and additive manufacturing (AM).[5,6] AM technology enables effective control over the structure and properties of materials, resulting in HEAs with enhanced strength, durability, and thermal stability compared to those of the conventional manufacturing process.[7] In addition, AM technology is environmentally sustainable as it minimizes the wastage of raw materials.[8,9]

Selective laser melting (SLM) technology is one of the most promising AM techniques, enabling the direct fabrication of various complex parts with a precise and uniform microstructure. Notably, selecting the appropriate raw material powder is crucial in enhancing the quality and efficiency of the finished parts in SLM. The SLM process requires powder particles ranging from 15 to 53 μm in size, with good sphericity, excellent flowability, and high tap density.[10] Nowadays, gas atomization (GA), mechanical alloying (MA), and plasma rotating electrode processing (PREP) are the primary methods for developing powders. However, a challenge arises from the presence of a significant number of satellite powder particles and hollow powder in GA-prepared HEA powders, both adversely impacting print quality. Additionally, MA-prepared HEA powders exhibit low sphericity, necessitating subsequent spheroidization processes to meet the powder requirements for AM.[11,12] Although satellite powder can also be produced through PREP preparation, it can be greatly reduced through the sieving and optimization of process parameters. Among these preparation methods, the powder prepared by PREP exhibits advantages such as good sphericity, low oxygen content, a narrower particle size distribution (PSD), and a smooth surface, which meet the basic requirements of raw material powders in SLM.[13] However, the main drawbacks of PREP are coarse particle size and low yield of fine powder, which limits its application in the field of AM. Furthermore, differences in the density, surface tension, and solidification temperature of different materials as well as changes in the powdering process can lead to variations in powder properties. Therefore, it is imperative to investigate the relationship between PREP parameters and powder particle size as well as performance, so as to explore the impact of powder particle size on the microstructure. The fabrication of pre-alloyed $Ni_{41}Al_{41}Cr_{12}Co_6$ spherical powder produced using the PREP technology was investigated. The results demonstrate that the powders exhibit enhanced properties for AM applications.[14] Furthermore, the AM

Received: January 9, 2024
Revised: March 21, 2024
Accepted: March 28, 2024
Published: April 11, 2024

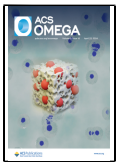

process of Inconel 718 powders produced by GA and PREP was analyzed, respectively.[15] The results indicated that PREP powders possess a smooth surface, spherical shape, higher bulk density, and improved flowability compared to GA powder, resulting in more stable mechanical properties of molded parts.

In recent years, $Al_{0.5}CoCrFeNi$ HEA has attracted significant attention and research from numerous scholars due to its favorable corrosion resistance, excellent high-temperature properties, and superior mechanical properties. However, the performance of $Al_{0.5}CoCrFeNi$ HEA still relies on the powder quality, which subsequently impacts the performance of molded parts.[16−21] Regarding the excellent performance of the $Al_{0.5}CoCrFeNi$ HEA, PREP was used to prepare high-quality $Al_{0.5}CoCrFeNi$ HEA powder for potential use in AM (especially SLM) in the present investigation. The microstructure and chemical composition of the powder were characterized. Furthermore, the role of powder particle diameter on the relationship between the secondary dendrite arm spacing (SDAS) and cooling rate will also be analyzed.

2. EXPERIMENTAL MATERIALS AND METHODS

The $Al_{0.5}CoCrFeNi$ HEA powder was produced by PREP with the SL-ZFW-04 equipment (Sailong, China). The alloy electrode bar was composed of Al, Co, Cr, Fe, and Ni in a molar ratio of 1:2:2:2:2, respectively. To optimize the preparation process, a series of experiments were conducted to investigate the effect of different rotational speeds and currents on the powder properties. Detailed experimental results can be found in the Supporting Information. Based on these experiments, rotational speed of 35,000 rpm with 650 A current showed optimal particle distribution and morphology while achieving high properties, thus identifying this combination as the experiment process parameter.

The schematic of PREP is displayed in Figure 1. During the powdering procedure, the ends of the alloy electrode bar are

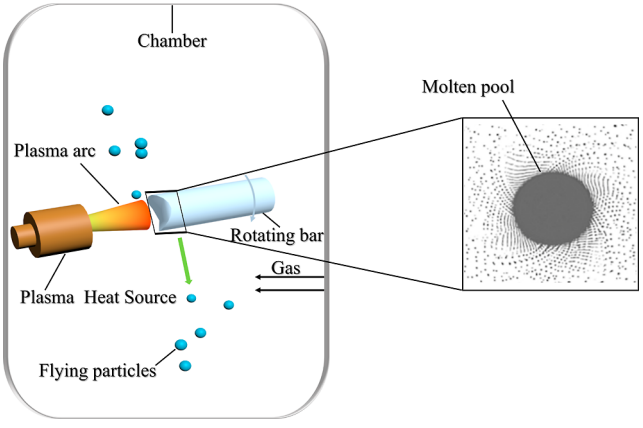

Figure 1. Illustration of PREP.

melted under plasma heating, and the droplets are immediately separated from the alloy electrode bar when sufficient centrifugal force is obtained. Finally, the metal droplets rapidly solidify and cool to room temperature via an inert gas process. The parameters of the PREP prepared powder are listed in Table 1. The equipment chamber was filled with Ar inert protective gases and maintained at a working pressure of 0.15 MPa. The powder was sieved into size ranges of 25−50 μm, 50−75 μm, 75−100 μm, and >100 μm. The PSD and sphericity of powder was measured using a laser particle size

Table 1. Parameters of the PREP-Prepared Powder

name	symbol and unit	value
diameter of the electrode bar	d (mm)	30
length of the electrode bar	l (mm)	600
rotating speed of the electrode bar	n (rpm)	35000
working plasma current	i (A)	650

analyzer (Mastersizer 3000E, Malvern, U.K.). The phases were determined by X-ray diffraction (XRD, DRON-3, Burevestnik, Russia) using Cu as the X-ray source, with a scanning range of 10−90° and a scanning speed of $4°\cdot min^{-1}$. The powder was inlaid and then mechanically polished and etched with aqua regia. Microstructure and chemical composition of the powder surface were analyzed using scanning electron microscopy (SEM, SU5000, Hitachi, Japan) with energy-dispersive spectroscopy (EDS) capability and X-ray photoelectron spectroscopy (XPS). Image Pro Plus software was used to measure SEM images of powder cross sections ranging from 10 to 200 μm to quantify the SDAS. To obtain a representative value of the SDAS for each cross-section, multiple measurements of the SDAS were conducted within a single cross-section, and the representative value was represented by calculating the average of the selected measurements. In order to ensure accuracy and reproducibility, consistency measures were taken in selecting measurement points and calculating averages. Additionally, a sufficient number of measurements were conducted to minimize the influence of random errors. The flowability of the powder was determined by using a powder flow tester (BT100, Bettersize, China). 50 g of powder was poured into a blocked funnel, then open the bottom entrance of the funnel and record the time it takes for all of the powder to completely flow out. The tap density of the powder was measured by using a compaction density tester (ZX-201, Bettersize, China). The powder (50 g) was placed in a measuring cylinder, which was fixed to the apparatus and vibrated at a frequency of 200 Hz for 5 min. The oxygen content of the powder was detected using an oxygen and nitrogen analyzer (ON736, Leco, USA).

3. RESULTS AND DISCUSSION

3.1. Analysis of the Powder Morphology. The morphology (Figure 2a) and PSD (Figure 2b) of the $Al_{0.5}CoCrFeNi$ HEA powder were characterized. Figure 2a illustrates that the $Al_{0.5}CoCrFeNi$ HEA powder exhibits high sphericity and minimal presence of satellite powder. PSD and average particle size (d_{50}) influence the quality of the AM products. A uniform PSD improves the flowability of the powder because the voids between particles of similar size are more consistent, reducing the resistance during the flow process. In addition, a smaller d_{50} results in a higher tap density, which improves the mechanical properties of the AM products. Two other key parameters of the PSD are d_{10} and d_{90}, which represent 10 and 90% of the total number of particles with a size smaller than this value. The PSD of the $Al_{0.5}CoCrFeNi$ HEA powder is displayed in Figure 2b. It can be seen that the powder prepared by PREP had a more uniform PSD. The characteristic particle size values of the powder were as follows: D_{10} = 21.2 μm, D_{50} = 38.7 μm, and D_{90} = 60.2 μm, indicating that the powder is suitable for AM.

Figure 3 shows the surface morphologies of the as-prepared powder. The morphologies of various particle size powders are displayed in Figure 3. Figure 3a,d shows that the $Al_{0.5}CoCrFeNi$ powder (102.9 μm) was spherical with a

https://doi.org/10.1021/acsomega.4c00291
ACS Omega 2024, 9, 18358−18365

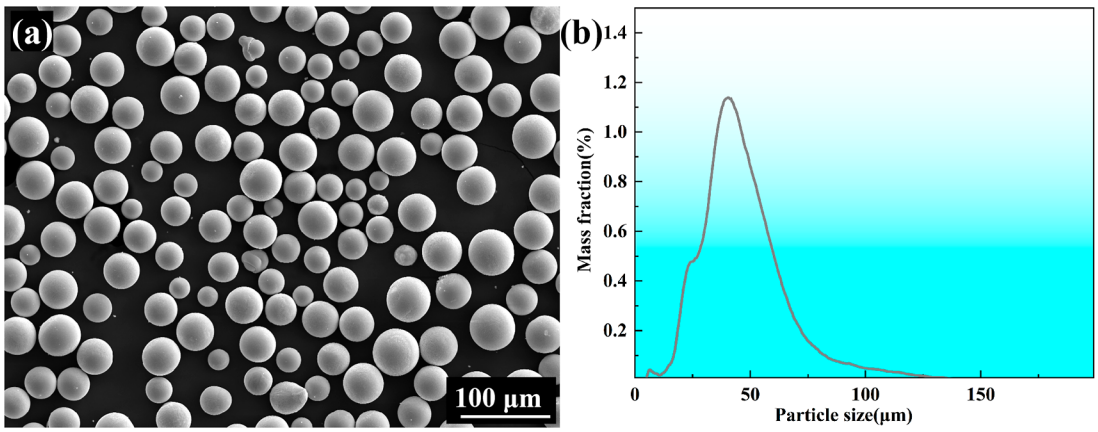

Figure 2. Morphology of the $Al_{0.5}CoCrFeNi$ powder (a) and the PSD (b).

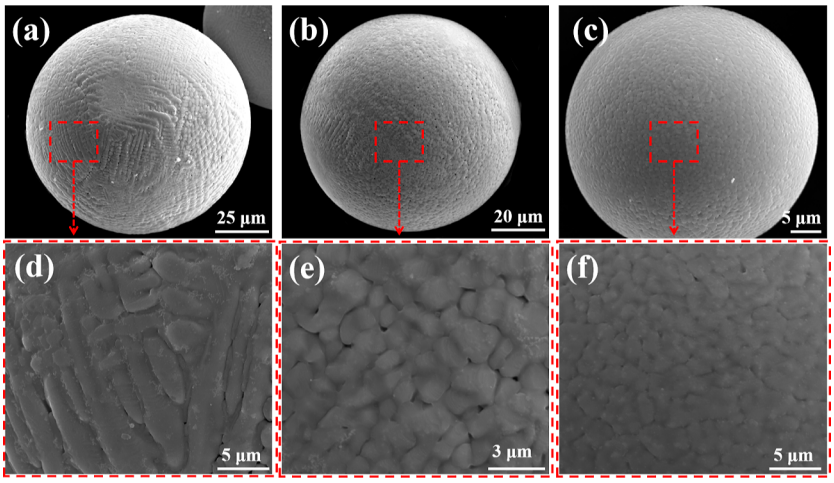

Figure 3. Surface morphology of the $Al_{0.5}CoCrFeNi$ powder: (a) 102.9 μm with the corresponding local magnification (d); (b) 62.3 μm with the corresponding local magnification (e); and (c) 32.1 μm with the corresponding local magnification (f).

rough surface, which was due to the solidification rate and surface tension of large particles. The slower solidification of powder with larger particle size leads to the adsorption of fine particles, resulting in a rough surface. Furthermore, the structure of the powder particle exhibits a combination of primary and radial dendrites with smaller second dendrite arms, which is attributed to the promotion of dendritic tissue formation by rapid cooling and solidification processes. Figure 3b,e exhibits a particle with a size of 62.3 μm, which had a smooth surface with significant voids and cell structure. This phenomenon aris due to the inverse relationship between PSD reduction and cooling rate enhancement. Figure 3c,f shows the microstructure of powder particles with a size of 32.1 μm. It can be observed that the powder exhibits equiaxed grain or featureless crystal.

The presence of a higher satellite powder and defective powder leads to the reduction of fluidity, which is detrimental to the quality of the AM product. Five SEM images were randomly selected for analysis, in which the percentage of satellite powder and irregular particles was less than 1%. The common defective powder particles of HEA powder made by PREP are displayed in Figure 4. The satellite powder was attached to the surface of particles with a particle size of approximately 110 μm (Figure 4a), resulting from smaller particles solidifying faster and being adsorbed onto larger particles during solidification. Proper adjustment of the

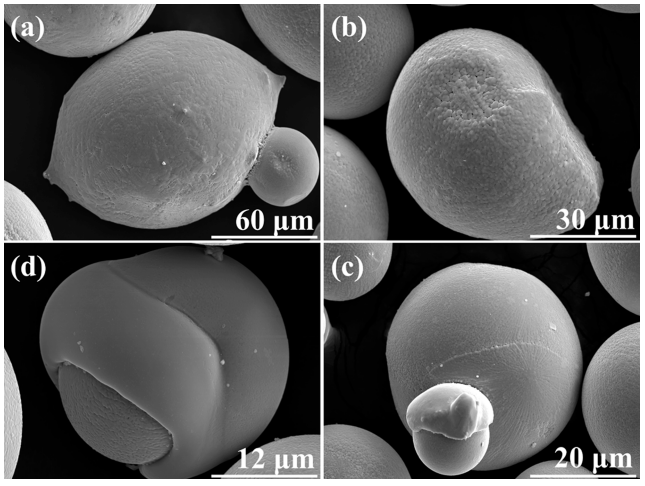

Figure 4. Morphologies of defective particles of the $Al_{0.5}CoCrFeNi$ HEA powder: (a) satellite powder; (b) nonspherical particle; (c) collision particle; and (d) irregular particle.

rotational speed can reduce the formation of satellite powder as it directly affects droplet separation and the solidification rate. Figure 4b shows the formation of nonspherical particles when molten droplets turned into flakes due to surface tension. Figure 4c shows the fine particle with a 35 μm particle size

https://doi.org/10.1021/acsomega.4c00291
ACS Omega 2024, 9, 18358−18365

embedded within a larger particle measuring 110 μm, which was ascribed to the collision between the solidified powder and the unconsolidated powder. The powder particles of different particle sizes have different trajectories in the PREP. The solidified powder will collide with the unconsolidated powder due to the overlap of trajectories. Reducing the generation of irregular powder can be achieved by varying the flow rate and type of cooling gas, which can affect the cooling rate and trajectory of the liquid metal droplets. Figure 4d exhibits the phenomenon of adsorption of small particle size powder by larger particle after collision. To enhance the overall efficiency of powder collection and minimize satellite powder accumulation, it is recommended to employ more precise collection equipment. Furthermore, implementing regular cleaning and maintenance of the equipment proves to be an effective strategy for reducing impurity and residue buildup.

3.2. Influence of Particle Diameter on the SDAS and Cooling Rate. The SDAS, as a crucial parameter of HEA, has a significant impact on its performance and applications. A smaller SDAS can enhance the strength and ductility of HEA. The SDAS can be effectively regulated by reasonable process control, so it needs to be studied in depth to understand its relationship with the particle diameter and cooling rate. The solidification microstructure of the powder is influenced by two apparent parameters during undercooling: the temperature gradient at the solid−liquid interface and the solidification rate of the solidification front. Under extreme undercooling conditions, dendrites change to cytosol or even a featureless smooth structure. Therefore, the solidification microstructure of the powder is highly dependent on the size of the powder particles. Cross-sectional solidification morphologies of the as-prepared powder are displayed in Figure 5.

Figure 5a shows that the $Al_{0.5}CoCrFeNi$ powder (93.3 μm) exhibited a dendritic structure. When the particle size was further reduced to 78.6 μm, the growth of secondary dendrites was inhibited due to increased supercooling, resulting in smaller dendrites and columnar crystals, as shown in Figure 5b.

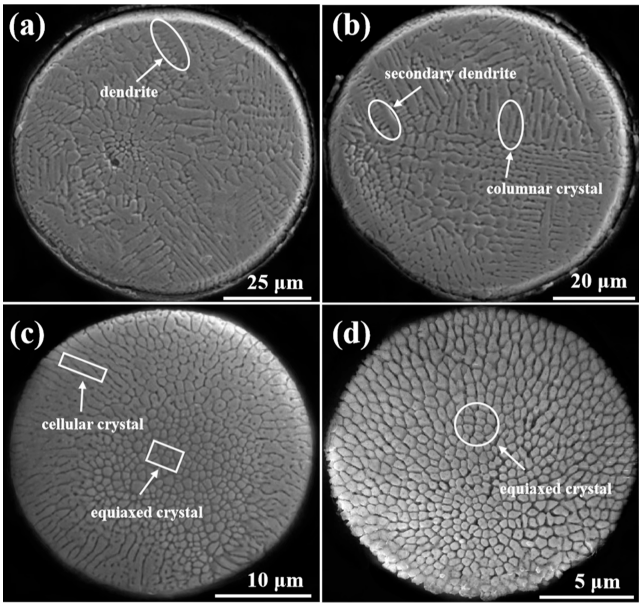

Figure 5. Cross-sectional morphologies of the $Al_{0.5}CoCrFeNi$ HEA powder with different particle sizes: (a) 93.3 μm; (b) 78.6 μm; (c) 31.6 μm; and (d) 16.7 μm.

Figure 5c shows that smaller cellular crystals can be found on the outer side, and equiaxial crystals can be observed in the cross-section of the powder particles. This is due to the different temperatures and cooling rates present on the outside and inside of the powder. As shown in Figure 5d, when the powder size was reduced to 16.7 μm, equiaxed crystals were observed. This is due to the increased contact area of the powder with the cooling gas, which lead to an increase in the cooling rate.

The alloy powder prepared by PREP has a high cooling rate, which can reach 10^2 to 10^6 K s^{-1}.[22] As shown in Figure 5, the particle size was largely responsible for the microstructure of the PREP $Al_{0.5}CoCrFeNi$ powder. However, the SDAS is usually reduced due to the reduction in the powder particle size. Moreover, the correlation between SDAS and the temperature gradient (G) and solidification rate (R) has been proposed by different theoretical approaches, as shown in eq 1.[23]

$$\mathrm{SDAS} \sim \left(\frac{1}{GR}\right)^{1/3} \tag{1}$$

In powder particles of sizes 25−50 μm, 50−75 μm, 75−100 μm , and >100 μm, the SDAS was measured as 0.14−0.37 μm, 0.37−0.63 μm, 0.63−0.89 μm, and >0.89 μm, respectively. Afterward, the function curve was acquired by linear fitting about the SDAS (λ) versus particle diameter (d), which is shown in Figure 6. The function of the SDAS in relation to particle diameter is as follows

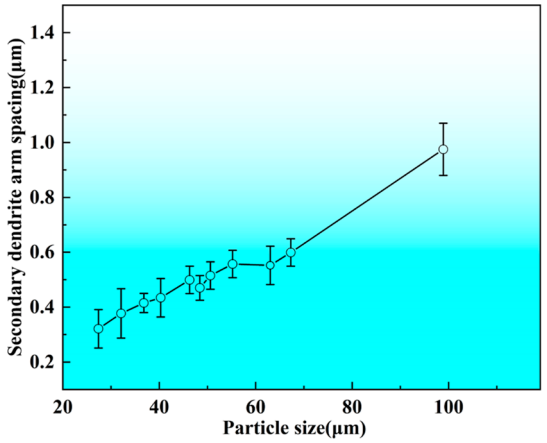

Figure 6. Relationship between SDAS and particle diameter.

$$\lambda = 0.01104d - 0.14 \tag{2}$$

The results indicate that the SDAS in the PREP $Al_{0.5}CoCrFeNi$ powder increases with an increasing particle size.

According to eq 1, the higher the cooling rate of the powder, the smaller the SDAS of the powder. In addition, according to eq 2, the smaller the SDAS, the smaller the particle size of the powder. Therefore, the cooling rate of the powder can be indirectly inferred by observing the particle size of the powder. The function between the cooling rate (v_c) and the powder diameter (d) is given as[24]

$$v_c = \frac{\mathrm{d}T_p}{\mathrm{d}t} = \frac{6h}{\rho C_p d}(T_d - T_f) \tag{3}$$

https://doi.org/10.1021/acsomega.4c00291
ACS Omega 2024, 9, 18358−18365

where T_p is the liquidus temperature for the $Al_{0.5}CoCrFeNi$ HEA; h indicates the interfacial heat transfer coefficient; C_p indicates the equivalent specific heat capacity; ρ indicates the density of the molten liquid droplet; T_d indicates the temperature of droplet; and T_f is the temperature of gas. The value of h can be obtained from the following equation from a previous study.[25] The values of C_p, ρ, T_d, and T_f refer to a previous report.[26]

$$h = \frac{2k_g}{d} + 0.6k_g\sqrt{\frac{U\rho_g}{\mu_g d}} \quad (4)$$

where k_g represents the thermal conductivity; d represents the droplet diameter; ρ_g represents the density of cooling gas; μ_g represents the dynamic viscosity of cooling gas; and U represents the relative velocity of droplets. The values of k_g, ρ_g, μ_g, and U refer to a previous report.[26,27]

During cooling in an argon atmosphere, if the actual temperature of the droplet exceeds the desired solidification temperature, then it must be reduced to a lower temperature for complete solidification. However, as the droplets are not superheated when they are first melted by the bar, the calculations assume that there is no supercooling during solidification of the droplets and that the temperature distribution is uniform. The velocity of the droplets is 73.3 m s^{-1}, calculated as $v = 2\pi rn$, where n is the rotational speed of the alloyed bar of 35,000 ppm and r is the radius of the rotating alloyed bar of 15 mm. The cooling rate of the droplets can be calculated from eqs 3 and 4 as follows

$$v_c = 4.34 \times 10^{-5} d^{-2} + 2.62 \times 10^{-2} d^{-3/2} \quad (5)$$

Figure 7 shows that the cooling rate of the $Al_{0.5}CoCrFeNi$ droplets with a diameter of less than 13 μm was ~10^6 K s^{-1},

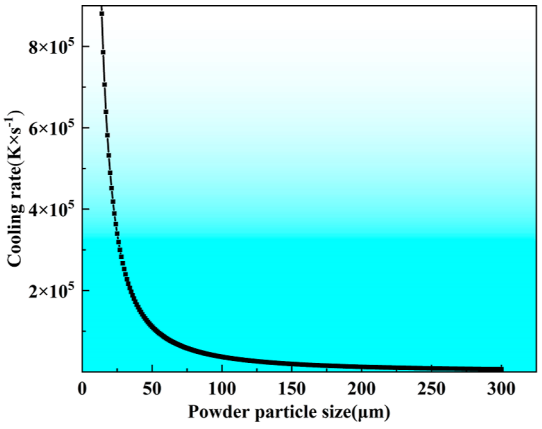

Figure 7. Relationship between the cooling rate and powder particle size.

which was the same as the cooling rate of the PERP droplet prepared in the previous study[28], ~10^6 K s^{-1}, with a diameter of 8 μm. Furthermore, it can be seen that the cooling rate dropped sharply from ~10^6 to ~10^5 K s^{-1} as the powder particle size increased from 13 to 53 μm, while the cooling rate remains within $10^{\sim 5}$ K s^{-1} as the particle size increased from 53 to 231 μm. The higher specific surface area may account for the high cooling rate of the smaller powder particles.

In summary, the relationship between the particle size and SDAS, as well as the cooling rate, was evaluated. It can be seen that reducing the particle size leads to a decrease in the SDAS while simultaneously increasing its specific surface area, thereby accelerating the cooling rate. These factors collectively contribute to the reduction of SDAS. In PREP, augmenting rotational speed and current intensity can effectively diminish particle size, thus achieving the objective of reducing the SDAS.

3.3. Phase Structure and Chemical Analysis of the PREP $Al_{0.5}CoCrFeNi$ HEA Powder. The XRD patterns of powder particles with different particle sizes are displayed in Figure 8. The powder is mainly composed of a bcc + fcc duplex

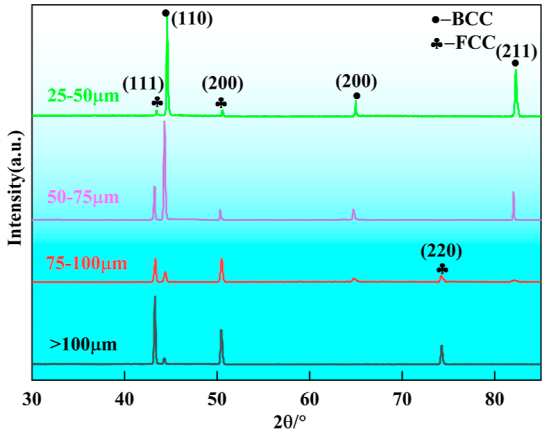

Figure 8. XRD patterns of the PREP $Al_{0.5}CoCrFeNi$ HEA powder according to the PSD.

solid solution from the main diffracted peaks corresponding to (111), (110), (200), and (211) of XRD patterns. This phenomenon is similar to the results in previous studies[29] on phase constituents of powder prepared by GA. Furthermore, there is a significant correlation between the phase composition and the particle size, as observed from the XRD patterns of the powder. The fcc solid solution was formed in powder with a particle size greater than 100 μm. However, the powder was mainly composed of the fcc + bcc duplex solid solution phase when the particle size decreased to 50−100 μm. The powder primarily consisted of a major bcc phase and minor fcc phase when the powder particle size was reduced to 25−50 μm. This is due to the reduction in the particle size, which leads to an increase in the cooling rate of the powder. The higher cooling rate reduces the time for crystal nucleation and growth during solidification, which may contribute to the formation of the bcc phase. In addition, the solid solubility between different elements is limited, and the higher cooling rate restricts diffusion between the elements, inhibiting the formation of the fcc phase.

The distribution of elements in the cross-section of powder should be carefully considered due to the complex chemical composition of the $Al_{0.5}CoCrFeNi$ powder. The elemental map distributions of Al, Co, Cr, Fe, and Ni in the PREP $Al_{0.5}CoCrFeNi$ powder were obtained randomly, as illustrated in Figure 9. The results of EDS analyses of the powder showed that the elemental contents of Al, Co, Cr, Fe, and Ni are 12.70, 20.40, 23.30, 22.09, and 24.03%, respectively, indicating that the $Al_{0.5}CoCrFeNi$ HEA powder with a uniform chemical composition can be produced by PREP.

AM products often produce highly inhomogeneous grains and chemically biased microstructures, which are more common in HEAs. Therefore, it is essential to confirm the

https://doi.org/10.1021/acsomega.4c00291
ACS Omega 2024, 9, 18358−18365

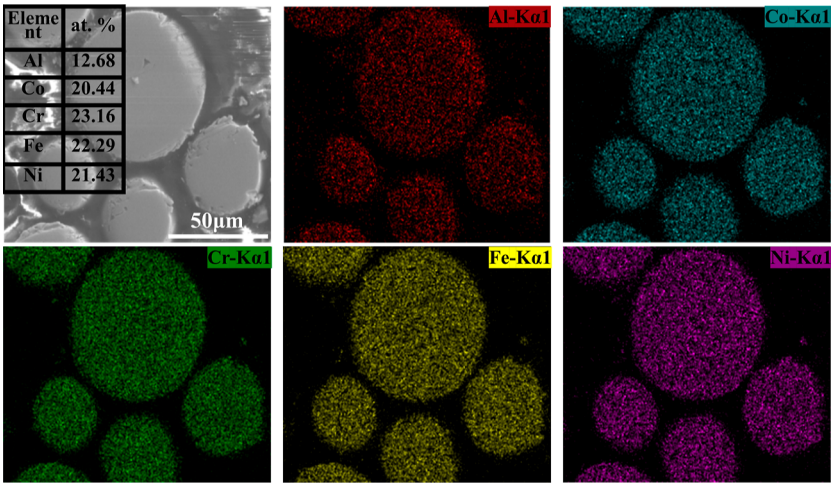

Figure 9. EDS analysis and elemental map distribution of the PREP $Al_{0.5}CoCrFeNi$ powder.

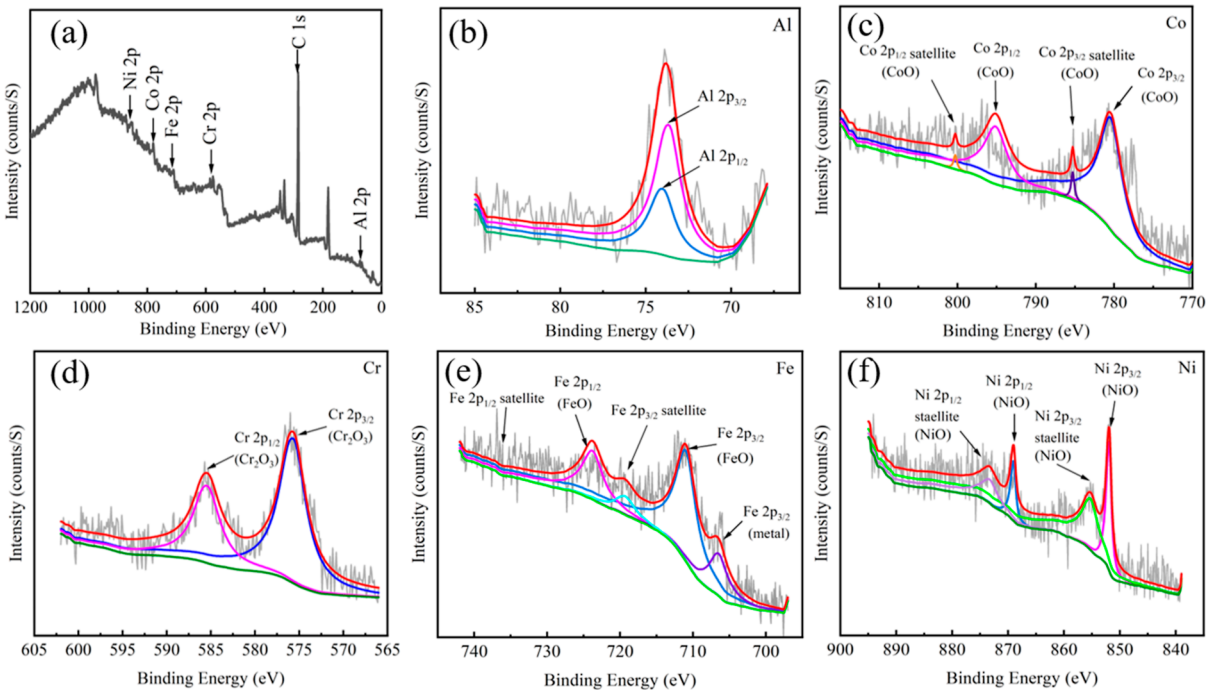

Figure 10. XPS electron spectra of the PREP $Al_{0.5}CoCrFeNi$ HEA powder: (a) full spectrum; (b) Al 2p; (c) Co 2p; (d) Cr 2p; (e) Fe 2p; and (f) Ni 2p.

elements distribution on the surface of the HEA powder produced by PREP. The elemental composition, chemical state, and molecular structure of the surface compounds of the $Al_{0.5}CoCrFeN$ powder were investigated by XPS analysis, as shown in Figure 10. Al $2p_{3/2}$ and Al $2p_{1/2}$ represent the peaks of Al in the metal phase. In addition, two peaks of Co 2p at 779.8 and 795.7 eV were observed, as shown in Figure 10c, revealing that Co oxide is mainly in the form of Co^{2+}. Furthermore, the peaks for Fe showed both metallic and oxidative contributions, while the peaks for Cr and Ni showed only oxidative contributions.

3.4. Oxygen Analysis of the PREP $Al_{0.5}CoCrFeNi$ HEA Powder. If the powder particles prepared by PREP are exposed to air, they will quickly adsorb detrimental impurities, such as oxygen, resulting in an elevation in the oxygen content of the powder. Powders with a high oxide content may lead to deterioration of the mechanical properties of the AM product, which is due to the fact that higher oxides may lead to local defects. The most effective way to reduce the oxygen content is by minimizing exposure to oxygen as much as possible. First, the pretreatment process should be carried out under a vacuum or inert atmosphere to reduce residual oxygen levels. Second, the preparation process should also be conducted within a vacuum environment, thereby significantly reducing the overall powder oxygen content. The oxygen content of the powder is shown in Figure 11. The results demonstrated that the oxygen contents of powder particles with particle size >100, 75−100, 50−75, and 25−50 μm were 104, 107, 172, and 296 ppm, respectively. The oxygen content of the PREP powder is similar to that of the GA powder.[30] The obtained result indicates that the $Al_{0.5}CoCrFeNi$ HEA powder prepared by PREP has a lower oxygen content and is suitable for the AM.

https://doi.org/10.1021/acsomega.4c00291
ACS Omega 2024, 9, 18358−18365

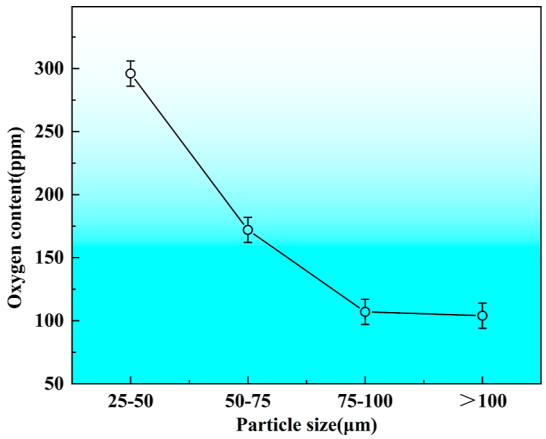

Figure 11. Oxygen content of the PREP $Al_{0.5}CoCrFeNi$ HEA powder.

The sphericity of the $Al_{0.5}CoCrFeNi$ HEA powder produced by PREP exceeded 94% due to its immunity to the influence of applied airflow during solidification. In addition, the low probability of powder collision suggests that trajectories do not easily coincide under high centrifugal forces. Furthermore, flowability and tap density of powder are important processing properties that determine their suitability for AM technology. The spherical $Al_{0.5}CoCrFeNi$ powder was characterized by a tap density of 4.76 g·cm^{-3} and an excellent flow rate of 15.01 s·50 g^{-1}, which has the ability to enhance the performance of AM products.

The yield of powder produced by the PREP is significantly influenced by the size of the equipment, the material processed, and the operating parameters, ranging from a few hundred grams to several kilograms. The production of powder is listed in Table 2; the productivity of the powder reached

Table 2. Productivity of PREP

weight of bar	weight of powder	weight of remnant electrode bar	productivity of powder
662.5 g	504.5 g	157.2 g	76.2%

76.2% and the actual amount of powder produced per batch was 157.2 g. Considering the high demand for powder in powder bed fusion technology, it is especially critical to increase the yield of PREP. To enhance yield without compromising quality, productivity improvements can be realized through the optimization of the operating parameters. Specifically, fine-tuning of parameters such as the electrode rotation speed and the plasma gas flow rate are crucial for refining the production process and boosting the powder production rate. Furthermore, the transition from a batch to a continuous operation mode facilitates a seamless powder production process. This is achieved by consistently feeding the electrode material and systematically collecting the powder produced, thereby significantly elevating the overall output.

4. CONCLUSIONS

In this paper, the PSD of the spherical $Al_{0.5}CoCrFeNi$ HEA powder prepared by PREP was investigated, and the defective powder was characterized. The impacts of particle size on the SDAS and cooling rate were analyzed. Furthermore, the influence of powder particle size on microstructure, phase constituents, and chemical composition has been elucidated, and the main conclusions are as follows:

(1) A $Al_{0.5}CoCrFeNi$ HEA powder with size ranging from 15 to 140 μm was produced. The characteristic particle size values of the powder were as follows: D_{10} = 21.2 μm, D_{50} = 38.7 μm, and D_{90} = 60.2 μm. The solidification structure is related to the particles size, where larger particles exhibit a dendritic structure while smaller particles display a cellular, equiaxed crystal structure.

(2) The relationship between particle size and SDAS, as well as cooling rate, was evaluated as follows: $\lambda = 0.0105d + 0.062$ and $v_c = 4.34 \times 10^{-5}d^{-2} + 2.62\times10^{-2}d^{-3/2}$, respectively.

(3) The reduction in particle size led to an increase in the bcc phase and a decrease in the fcc, which is reflected in the predominance of the fcc + bcc phase in powder larger than 100 μm, and the predominance of the bcc phase in powder ranging from 25 to 50 μm, with a small amount of the fcc phase present.

(4) The $Al_{0.5}CoCrFeNi$ HEA powder exhibits excellent properties with a tap density of 4.76 g cm^{-3}, flowability of 15.01 s 50 g^{-1}, oxygen content below 300 ppm, and sphericity exceeding 94%. It is expected to be used in AM, particularly in SLM.

The HEA powders produced by PREP have been widely used in the aerospace, shipbuilding, and biomedical fields. Exploring ways to prepare HEA powders with varying compositions by PREP, studying in depth the relationship between the performance of the powders and their microstructure, and evaluating their applicability are expected to further promote the development of the AM industry.

■ ASSOCIATED CONTENT

Supporting Information

The Supporting Information is available free of charge at https://pubs.acs.org/doi/10.1021/acsomega.4c00291.

Optimization of the PREP process; key particle indicator; particle size, sphericity, yield, and morphology of the PREP powder at different conditions; and physical properties (PDF)

■ AUTHOR INFORMATION

Corresponding Authors

Yicheng Feng − *School of Materials Science and Chemical Engineering, Harbin University of Science and Technology, Harbin 150080, China*; Email: fyc7806067@163.com

Yang Xie − *Institute of Advanced Technology, Heilongjiang Academy of Science, Harbin 150000, China*; Email: xyy89650641@126.com

Authors

Yanchun Li − *Institute of Advanced Technology, Heilongjiang Academy of Science, Harbin 150000, China*; orcid.org/0009-0003-3595-164X

Yi Sui − *School of Materials Science and Chemical Engineering, Harbin University of Science and Technology, Harbin 150080, China*

Yu Zhang − *Institute of Advanced Technology, Heilongjiang Academy of Science, Harbin 150000, China*

Yan Li − *Institute of Advanced Technology, Heilongjiang Academy of Science, Harbin 150000, China*

Meihui Song − *Institute of Advanced Technology, Heilongjiang Academy of Science, Harbin 150000, China*

https://doi.org/10.1021/acsomega.4c00291
ACS Omega 2024, 9, 18358−18365

Shulin Gong − *Institute of Advanced Technology, Heilongjiang Academy of Science, Harbin 150000, China*

Complete contact information is available at: https://pubs.acs.org/10.1021/acsomega.4c00291

Notes

The authors declare no competing financial interest.

■ ACKNOWLEDGMENTS

This work was supported by the Heilongjiang Academy of Science (YZ2023GJS01) and the Heilongjiang Provincial Finance Department (ZNBZ2022GJS01).

■ REFERENCES

(1) Yeh, J. W.; Chen, S. K.; Lin, S. J.; Gan, J. Y.; Chin, T. S.; Shun, T. T.; Tsau, C. H.; Chang, S. Y. Nanostructured High-Entropy Alloys with Multiple Principal Elements: Novel Alloy Design Concepts and Outcomes. *Adv. Eng. Mater.* **2004**, *6* (5), 299−303.

(2) Arif, Z. U.; Khalid, M. Y.; Al Rashid, A.; ur Rehman, E.; Atif, M. Laser deposition of high-entropy alloys: A comprehensive review. *Opt. Laser Technol.* **2022**, *145*, 107447.

(3) George, E. P.; Raabe, D.; Ritchie, R. O. High-Entropy Alloys. *Nat. Mater.* **2019**, *4*, 515−534.

(4) Chang, X. J.; Zeng, M. Q.; Liu, K. L.; Fu, L. Phase Engineering of High-Entropy Alloys. *Adv. Mater.* **2020**, *32* (14), 1907226.

(5) Zhang, Y.; Zuo, T. T.; Tang, Z.; Gao, M. C.; Dahmen, K. A.; Liaw, P. K.; Lu, Z. P. Microstructures and properties of high-entropy alloys. *Prog. Mater. Sci.* **2014**, *61*, 1−93.

(6) Tokarewicz, M.; Grądzka-Dahlke, M. Review of Recent Research on AlCoCrFeNi High-Entropy Alloy. *Met.* **2021**, *11* (8), 1302.

(7) Ren, J.; Zhang, Y.; Zhao, D.; Chen, Y.; Guan, S.; Liu, Y.; Liu, L.; Peng, S.; Kong, F.; Poplawsky, J. D.; Gao, G.; et al. Strong yet ductile nanolamellar high-entropy alloys by additive manufacturing. *Nature* **2022**, *608*, 62−68.

(8) Zhang, W.; Chabok, A.; Kooi, B. J.; Pei, Y. T. Additive manufactured high entropy alloys: A review of the microstructure and properties. *Mater. Des.* **2022**, *220*, 110875.

(9) Han, C. J.; Fang, Q. H.; Shi, Y. S.; Tor, S. B.; Chua, C. K.; Zhou, K. Recent Advances on High-Entropy Alloys for 3D Printing. *Adv. Mater.* **2020**, *32* (26), 1903855.

(10) Brandl, E.; Heckenberger, U.; Holzinger, V.; Buchbinder, D. Additive manufactured $AlSi_{10}Mg$ samples using selective laser melting(SLM): Micro-structure, high cycle fatigue, and fracture behavior. *Mater. Des.* **2012**, *34*, 159−169.

(11) Makhmutov, T.; Razumov, N.; Kim, A.; Ozerskoy, N.; Mazeeva, A.; Popovich, A. Synthesis of $CoCrFeNiMnW_{0.25}$High-Entropy Alloy Powders by Mechanical Alloying and Plasma Spheroidization Processes for Additive Manufacturing. *Met. Mater. Int.* **2021**, *27*, 50−54.

(12) Cui, Y. J.; Zhao, Y. F.; Numata, H.; Yamanaka, K.; Bian, H. K.; Aoyagi, K.; Chiba, A. Effects of process parameters and cooling gas on powder formation during the plasma rotating electrode process. *Powder Technol.* **2021**, *393*, 301−311.

(13) Chen, G.; Zhao, S. Y.; Tan, P.; Wang, J.; Xiang, C. S.; Tang, H. P. A comparative study of Ti-6Al-4V powders for additive manufacturing by gas atomization, plasma rotating electrode process and plasma atomization. *Powder Technol.* **2018**, *333*, 38−46.

(14) Kaplanskii, Y. Y.; Zaitsev, A. A.; Sentyurina, Z. A.; Levashov, E. A.; Pogozhev, Y. S.; Loginov, P. A.; Logachev, I. A. The structure and properties of pre-alloyed NiAl-Cr(Co, Hf) spherical powders produced by plasma rotating electrode processing for additive manufacturing. *J. Mater. Res. Technol.* **2018**, *7* (4), 461−468.

(15) Ruan, G.; Liu, C.; Qu, H.; Guo, C.; Li, G.; Li, X.; Zhu, Q. A comparative study on laser powder bed fusion of IN718 powders produced by gas atomization and plasma rotating electrode process. *Mater. Sci. Eng. A* **2022**, *850*, 143589.

(16) Guo, T.; Li, J. S.; Wang, J.; Wang, W. Y.; Liu, Y.; Luo, X. M.; Kou, H. C.; Beaugnon, E. Microstructure and properties of bulk $Al_{0.5}CoCrFeNi$ high-entropy alloy by cold rolling and subsequent annealing. *Mater. Sci. Eng. A* **2018**, *729* (27), 141−148.

(17) Miracle, D. B.; Senkov, O. N. A critical review of high entropy alloys and related concepts. *Acta Mater.* **2017**, *122*, 448−511.

(18) Du, Y. H.; Guo, C. H.; Jiang, F. C.; Li, Y. C.; Sun, X. J.; Sun, Q. F.; Zhang, H. X.; Dong, T.; Konovalov, S. Effect of heat treatment on microstructure and properties of $Al_{0.5}CoCrFeNi$ high entropy alloy fabricated by selective laser melting. *Mater. Sci. Eng. A* **2023**, *882*, 145466.

(19) Sun, Z. J.; Tan, X. P.; Wang, C. C.; Descoins, M.; Mangelinck, D.; Tor, S. B.; Jagle, E. A.; Zaefferer, S.; Raabe, D. Reducing hot tearing by grain boundary segregation engineering in additive manufacturing: example of an $Al_xCoCrFeNi$ high-entropy alloy. *Acta Mater.* **2021**, *204*, 116505.

(20) Sun, K.; Peng, W. X.; Yang, L. L.; Fang, L. Effect of SLM Processing Parameters on Microstructures and Mechanical Properties of $Al_{0.5}CoCrFeNi$ High Entropy Alloys. *Met.* **2020**, *10* (2), 292.

(21) Peyrouzet, F.; Hachet, D.; Soulas, R.; Navone, C.; Godet, S.; Gorsse, S. Selective Laser Melting of $Al_{0.3}CoCrFeNi$ High-Entropy Alloy: Printability, Microstructure, and Mechanical Properties. *J. Occup. Med.* **2019**, *71*, 3443−3451.

(22) Caccuri, V.; Cormier, J.; Desmorat, R. γ'-Rafting mechanisms under complex mechanical stress state in Ni-based single crystalline superalloys. *Mater. Des.* **2017**, *131*, 487−497.

(23) Fife, J. L.; Voorhees, P. W. The morphological evolution of equiaxed dendritic microstructuresduringcoarsening. *Acta Metall.* **2009**, *57* (8), 2418−2428.

(24) Zhang, L.; Liu, H. S.; He, X. B.; Din, R. U.; Qu, X. H.; Qin, M. L.; Li, Z.; Zhang, G. Q. Thermal evolution behavior of carbides and γ' precipitates in FGH96superalloy powder. *Mater. Charact.* **2012**, *67*, 52−64.

(25) Zuo, Z. B.; Hu, R.; Luo, X.; Wang, Q. X.; Li, C. X.; Zhu, Z.; Lan, J.; Liang, S. J.; Tang, H. K.; Zhang, K. Solidification Behavior and Microstructures Characteristics of Ti-48Al-3Nb-1.5Ta Powder Produced by Supreme-Speed Plasma Rotating Electrode Process. *Acta Metall. Sin.* **2023**, *36*, 1221−1234.

(26) Chou, H. P.; Chang, Y. S.; Chen, S. K.; Yeh, J. W. Microstructure, thermophysical and electrical properties in $Al_xCoCrFeNi$ ($0 \leq x \leq 2$) high-entropy alloys. *Mater. Sci. Eng. B* **2009**, *163* (3), 184−189.

(27) Zheng, M. Y.; Zhang, S. M.; Hu, Q.; He, H. J.; Sheng, Y. W.; Zhao, X. M. Microstructural characterisation of CuAgZr powder particles produced by argon gas atomisation. *Powder Metall.* **2018**, *61* (3), 231−240.

(28) He, W. W.; Liu, Y.; Tang, H. P.; Li, Y. P.; Liu, B.; Liang, X. P.; Xi, Z. P. Microstructural characteristics and densification behavior of high-NbTiAl powder produced by plasma rotating electrode process. *Mater. Des.* **2017**, *132* (15), 275−282.

(29) Zhou, S. C.; Zhang, P.; Xue, Y. F.; Wang, F. C.; Wang, L.; Cao, T. Q.; Tan, Z.; Cheng, B. y.; Wang, B. P. Microstructure evolution of $Al_{0.6}CoCrFeNi$ high entropy alloy powder prepared by high pressure gas atomization. *Trans Nonferrous Met. Soc. China.* **2018**, *28* (5), 939−945.

(30) Lee, Y.; Nagarjuna, C.; Song, J. W.; Jeong, K. Y.; Song, G.; Lee, J.; Lee, J. H.; Hong, S. J. Powder characteristics of $Al_{0.5}CoCrFeMnNi$ high-entropy alloys fabricated by gas atomisation method. *Powder Metall.* **2021**, *64* (3), 219−227.